

Nusselt number scaling in horizontal convection: boundary conditions and dimensionality

Navid C. Constantinou¹†, Cesar B. Rocha², Stefan G. Llewellyn Smith^{3, 4}, and William R. Young⁴

¹Research School of Earth Sciences & ARC Centre of Excellence for Climate Extremes, Australian National University, Canberra, ACT 2601, Australia

²Department of Marine Sciences, University of Connecticut, Groton, CT 06340, USA

³Department of Mechanical and Aerospace Engineering, University of California San Diego, La Jolla, CA 92093-0411, USA

⁴Scripps Institution of Oceanography, University of California San Diego, La Jolla, CA 92093-0213, USA

(Received January 2023)

We conduct a numerical study of horizontal convection (HC) at Prandtl number $Pr = 1$, with both no-slip and free-slip boundary conditions. We obtain 2D and 3D solutions and determine the relation between the Rayleigh number Ra and the Nusselt number Nu . In 2D we vary Ra between 0 and 6.4×10^{13} . In the range $10^6 \lesssim Ra \lesssim 10^{10}$ the Nu - Ra relation is, apart from minor departures, in agreement with Rossby's scaling $Nu \sim Ra^{1/5}$. With Ra greater than about 10^{11} we find a 2D regime with $Nu \sim Ra^{1/4}$ over three decades, up to the highest 2D Ra . In 3D, with maximum $Ra = 3.2 \times 10^{11}$, we only find Rossby scaling regimes. These results apply to both viscous boundary conditions. The $Nu \sim Ra^{1/4}$ regime has a double boundary layer (BL): there is a thin BL with thickness $\sim Ra^{-1/4}$ inside a thicker BL with thickness $\sim Ra^{-1/5}$. The $Ra^{-1/4}$ BL thickness, which determines Nu , coincides with the Kolmogorov and Batchelor scales of HC.

Our numerical and theoretical results indicate that 3D HC is qualitatively and quantitatively similar to 2D HC. At the same Ra , the 3D Nu exceeds the non-turbulent 2D Nu by only 20%, i.e., there is very little 3D enhancement of heat transport. Boundary conditions are more important than dimensionality: the non-turbulent 2D free-slip solutions have larger Nu than 3D no-slip solutions. The mechanical energy power integral of HC implies that mean square vorticity of 3D HC is nearly equal to that of 2D HC at the same Ra . Thus vorticity amplification by vortex stretching does not operate in 3D HC.

1. Introduction

Horizontal convection (HC) is convection driven by imposing non-uniform heating and cooling along a single horizontal surface, such as the top of a rectangular enclosure; there is no flux of heat through the other boundaries (Hughes & Griffiths 2008). Oceanography is an important motivation for consideration of HC (Sandström 1908; Rossby 1965; Coman *et al.* 2006; Kuhlbrodt 2008), and in that connection the dependence of horizontal heat transport on the strength of buoyancy forcing applied at the ocean surface is a prime question. Buoyancy forcing is quantified via the horizontal-convective Rayleigh number, Ra , and horizontal heat transport by a suitably defined Nusselt number Nu (Rocha *et al.* 2020b).

HC is an interesting counterpoint to Rayleigh-Bénard convection because HC buoyancy transport in the interior of the domain cannot be easily interpreted as the vertical motion of thermal plumes. Instead, heat enters the fluid where the non-uniform heated surface is

† Email address for correspondence: navid.constantinou@anu.edu.au

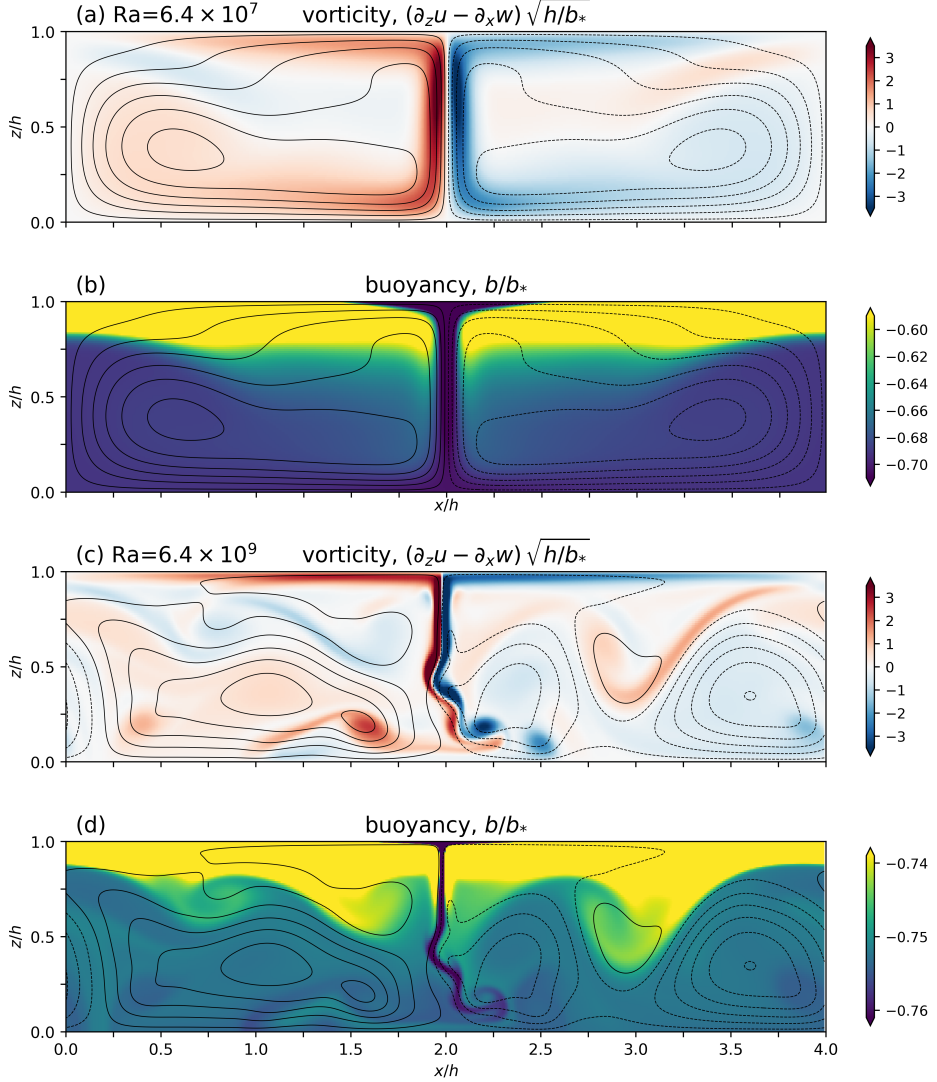


Figure 1: Snapshots of 2D free-slip HC at $\text{Ra} = 6.4 \times 10^7$ in panels (a) and (b) and $\text{Ra} = 6.4 \times 10^9$ in (c) and (d); $\text{Pr} = 1$. Contours are streamlines. At the top surface $-1 \leq b/b_* \leq +1$; the narrow range of the buoyancy color scale in (b) and (d) makes the small interior buoyancy variations visible. The sinusoidal surface buoyancy in (2.4) defines the buoyancy scale b_* ; h is the layer depth.

hotter than average and exits where it is colder. This horizontal transport is associated with a prominent boundary layer (BL) adjacent to the non-uniform surface.

The oldest result for the high- Ra variation of horizontal-convective Nu is the scaling law of Rossby (1965)

$$\text{Nu} \sim \text{Pr}^0 \text{Ra}^{1/5}, \quad (1.1)$$

where Pr is the Prandtl number. (Parameters Ra , Pr , and Nu are defined in section 2.) Figure 1 shows two numerical solutions in the Rossby-scaling regime (1.1).

Rossby (1965) was motivated by experiments, mainly with $\text{Pr} \sim 10^3$ and 10^4 , and their reasoning leading to (1.1) (reviewed in section 4) assumes visco-diffusive balances in the BL.

At moderately large Ra , the exponent 1/5 is supported by both laboratory work and numerical solutions (Rossby 1998; Mularney *et al.* 2004; Siggers *et al.* 2004; Wang & Huang 2005; Chiu-Webster *et al.* 2008; Sheard & King 2011; Ilicak & Vallis 2012). Perhaps because of Rossby’s assumption that the boundary layer is visco-diffusive, the scaling (1.1) is sometimes characterized as applying to steady laminar HC, e.g., the flow in figure 1(a) and (b). But (1.1) has much wider applicability: some studies find that the one-fifth law (1.1) applies in unsteady and three-dimensional (3D) HC regimes. For example, Gayen *et al.* (2014), with $Pr = 5$, find the exponent 1/5 in a steady 2D flow regime with $Ra \leq 10^{10}$, and also in a turbulent 3D regime with $Ra \geq 10^{12}$. In the transition, $10^{10} \leq Ra \leq 10^{12}$, the constant multiplying $Ra^{1/5}$ increases from 0.37 to 0.51. Gayen *et al.* (2014) make the important point that the exponent 1/5 also arises with a non-Rossby balance between inertia and buoyancy in the surface BL. In section 3 we provide further examples of (1.1) in unsteady three-dimensional regimes with $Pr = 1$. The tenacity of 1/5 as the primary exponent is striking, and rationalizes (1.1) in cases far removed from Rossby’s visco-diffusive scenario.

Increasing Ra , with Pr fixed, results in qualitative changes in the structure of HC: compare figure 2 with figure 1. It is unlikely that a single Nu – Ra power-law can persist across the six decades of Ra spanned by these illustrations. Tsai *et al.* (2020) have investigated 2D HC with $Pr = 6.14$ and no-slip boundary conditions. At moderately large Ra , say $10^8 < Ra < 10^{10}$, Tsai *et al.* (2020) find Rossby’s scaling law (1.1). But in the range $10^{10} < Ra < 10^{14}$, and provided that the imposed surface buoyancy varies linearly with the horizontal coordinate x , Tsai *et al.* (2020) report the scaling

$$Nu \sim Ra^{1/4}. \quad (1.2)$$

In section 3, using the sinusoidal surface buoyancy in (2.4), we also find the scaling (1.2) in a suite of 2D solutions at $Pr = 1$. We show that in 2D, with both no-slip and free-slip boundary conditions, (1.2) applies from about $Ra = 10^{11}$ to at least 6.4×10^{13} . In 3D, however, we achieve maximum $Ra = 3.2 \times 10^{11}$ and there is no numerical evidence for the one-fourth scaling (1.2).

The vortices evident in figure 2 indicate that the interior buoyancy fluctuations are so small that the interior dynamics is essentially that of a vortex gas characteristic of freely evolving 2D turbulence (Benzi *et al.* 1987, 1988; Carnevale *et al.* 1991; Dritschel *et al.* 2008; McWilliams 1984, 1990).

Tsai *et al.* (2020) note that the exponent one-fourth in (1.2) corresponds to one of the exponents proposed by Shishkina *et al.* (2016) in their phase diagram of the (Ra, Pr) parameter plane. We review the proposal of Shishkina *et al.* (2016) in sections 4 and 5, and conclude that this correspondence is accidental: diagnosis of the solutions in figure 2 does not confirm essential features of the one-fourth Ra – Nu scaling regimes in the phase diagram of Shishkina *et al.* (2016). In section 6 we suggest instead that scaling (1.2) follows if the thinnest BL has a thickness scaling as the Kolmogorov length. In section 7 we argue that our numerical results indicate that HC does not exhibit defining features of turbulence.

2. Formulation of the horizontal convection problem

We consider a Boussinesq fluid with density $\rho = \rho_0(1 - g^{-1}b)$, where ρ_0 is a constant reference density and b is the “buoyancy”. If, for example, the fluid is stratified by temperature variations then $b = g\alpha(T - T_0)$, where T_0 is a reference temperature and α is the thermal

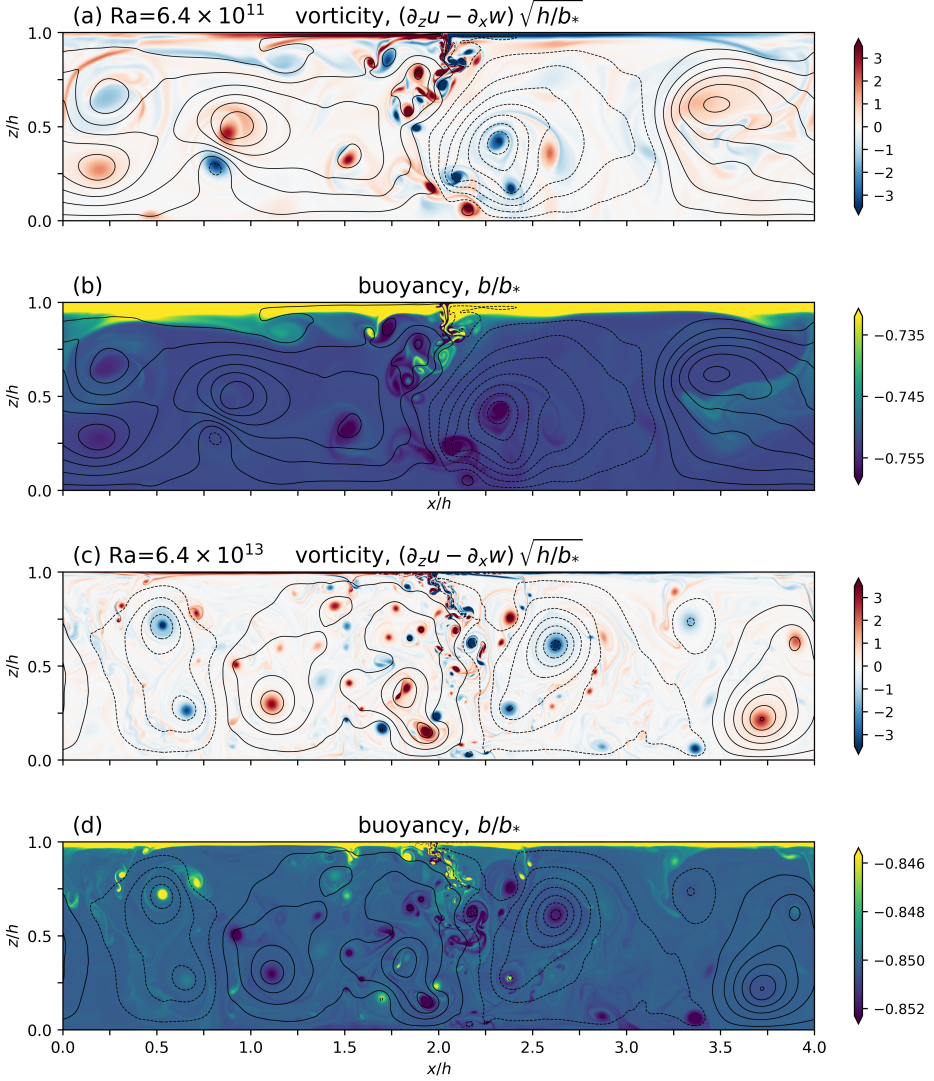


Figure 2: Snapshots of 2D free-slip solutions at $Ra = 6.4 \times 10^{11}$ in panels (a) and (b) and $Ra = 6.4 \times 10^{13}$ in (c) and (d); $Pr = 1$. Contours are streamlines. This illustration uses true aspect ratio so that axisymmetric vortices look circular. The buoyancy color scale is narrow in order to reveal the small interior buoyancy variations, which are localized within the cores of axisymmetric vortices. Across the six-decade range of Ra in figures 1 and 2 vorticity scales with $\sqrt{b_\star/h}$.

expansion coefficient. The Boussinesq equations of motion are

$$\mathbf{u}_t + \mathbf{u} \cdot \nabla \mathbf{u} + \nabla p = b\hat{\mathbf{z}} + \nu \nabla^2 \mathbf{u}, \quad (2.1)$$

$$b_t + \mathbf{u} \cdot \nabla b = \kappa \nabla^2 b, \quad (2.2)$$

$$\nabla \cdot \mathbf{u} = 0. \quad (2.3)$$

The kinematic viscosity is ν and the thermal diffusivity is κ .

2.1. Horizontal convective boundary conditions and control parameters

We suppose the fluid occupies a domain with depth h , length ℓ_x , width ℓ_y ; we assume periodicity in the x - and y -directions. At the bottom surface ($z = 0$) and top surface ($z = h$) the primary boundary conditions on the velocity, $\mathbf{u} = (u, v, w)$, is that $w = 0$; the viscous boundary condition is either no slip (**NS** hereafter), $u = v = 0$, or free slip (**FS** hereafter), $u_z = v_z = 0$. At the bottom $z = 0$ the buoyancy boundary condition is no flux, $\kappa b_z = 0$. At the top, $z = h$, the boundary condition is $b = b_s(x)$, where the top surface buoyancy b_s is a prescribed function of x . As a surface buoyancy field we use

$$b_s(x) = b_\star \cos kx, \quad (2.4)$$

where $k = 2\pi/\ell_x$.

As an idealization of conditions at the sea surface, **FS** is better than **NS**. But the main reason for considering different viscous boundary conditions is to test scaling arguments. We find only minor quantitative differences in the *Nu–Ra* scaling between the two boundary conditions. Thus scaling arguments that rely on special properties of **NS**, such as analogies with the Blasius BL, should be reconsidered: in the numerical solutions described below the main features of the *Nu–Ra* scaling relation are independent of the viscous boundary condition.

The problem is characterized by four non-dimensional parameters: the Rayleigh and Prandtl numbers

$$Ra \stackrel{\text{def}}{=} \frac{\ell_x^3 b_\star}{\nu \kappa}, \quad \text{and} \quad Pr \stackrel{\text{def}}{=} \frac{\nu}{\kappa}, \quad (2.5)$$

and the aspect ratios $A_x \stackrel{\text{def}}{=} \ell_x/h$ and $A_y \stackrel{\text{def}}{=} \ell_y/h$. With periodic boundary conditions in y (no side walls), 2D HC is the special case $A_y = 0$.

2.2. Mechanical energy dissipation

We use an overbar to denote an average over x , y , and t , taken at any fixed z and angle brackets $\langle \rangle$ to denote a total volume average over x , y , z , and t . Using this notation, we recall some results from [Paparella & Young \(2002\)](#) that are used below.

Horizontally averaging the buoyancy equation (2.2) we obtain the zero-flux constraint

$$\overline{wb} - \kappa \bar{b}_z = 0. \quad (2.6)$$

Taking $\langle \mathbf{u} \cdot (2.1) \rangle$, we obtain the kinetic energy power integral

$$\varepsilon = \langle wb \rangle, \quad (2.7)$$

where $\varepsilon \stackrel{\text{def}}{=} \nu \langle |\nabla \mathbf{u}|^2 \rangle$ is the rate of dissipation of kinetic energy and $\langle wb \rangle$ is rate of conversion between potential and kinetic energy.

Vertically integrating (2.6) from $z = 0$ to h , and using the fact that $\bar{b}_s = 0$, we obtain another expression for $\langle wb \rangle$; substituting this into (2.7) we find

$$\varepsilon = -\frac{\kappa \bar{b}(0)}{h}. \quad (2.8)$$

In (2.8), $\bar{b}(0)$ is the (x, y, t) -average of the buoyancy at the bottom $z = 0$.

2.3. The Nusselt number of horizontal convection

Following [Rocha et al. \(2020b\)](#), we use the dissipation of buoyancy variance,

$$\chi \stackrel{\text{def}}{=} \kappa \langle |\nabla b|^2 \rangle, \quad (2.9)$$

to define the Nusselt number as

$$Nu \stackrel{\text{def}}{=} \chi / \chi_{\text{diff}}. \quad (2.10)$$

Above, $\chi_{\text{diff}} \stackrel{\text{def}}{=} \kappa \langle |\nabla b_{\text{diff}}|^2 \rangle$ is the buoyancy dissipation of the diffusive solution, i.e., $\kappa \nabla^2 b_{\text{diff}} = 0$ with b_{diff} satisfying the same boundary conditions as b .

Application of variational methods to HC (Siggers *et al.* 2004; Winters & Young 2009; Rocha *et al.* 2020a) results in bounds on χ taking the form $Nu \lesssim Ra^{1/3}$. The exponent 1/3 is safely larger than the exponents 1/5 and 1/4 reported in numerical studies of HC, including this work.

Rocha *et al.* (2020b) show that there is also a “surface Nusselt number”

$$Nu_s \stackrel{\text{def}}{=} \overline{b_s \kappa b_z(h)} / \overline{b_s \kappa b_{\text{diff}}(h)}. \quad (2.11)$$

Above, $\kappa b_z(h)$ is the buoyancy flux through the top surface $z = h$. With sufficient temporal averaging $Nu = Nu_s$; in physical terms the interior entropy production, χ , is balanced by entropy flux through the surface $z = h$; Nu_s is the non-dimensional entropy flux though the surface. In numerical solutions described below, in which the temporal average is computed over a finite time interval, $Nu \approx Nu_s$ is a check on the estimated Nusselt number.

3. A numerical study of horizontal convection with $Pr = 1$

In this section we present the results of a numerical study directed at characterizing the variation of the Nusselt number Nu in (2.10) as a function of Ra . Computations are performed using Dedalus, a spectral framework for solving partial differential equations (Burns *et al.* 2020, www.dedalus-project.org). We use Fourier bases in the horizontal, periodic directions and a Chebyshev basis in the vertical; the equations are time stepped using a fourth-order implicit-explicit Runge–Kutta scheme.

We limit attention to $Pr = 1$ and the sinusoidal surface buoyancy forcing $b_s(x)$ in (2.4). We discuss both **NS** and **FS** boundary conditions and consider 2D solutions with aspect ratios

$$\ell_x/h = 4, \quad \ell_y/h = 0, \quad (3.1)$$

and 3D solutions with

$$\ell_x/h = 4, \quad \ell_y/h = 1. \quad (3.2)$$

Thus we have four solution suites: **2DFS**, **3DFS**, **2DNS**, and **3DNS**. The resulting estimates of Nusselt number are summarized in table 1 and figure 3.

3.1. The low- Ra regime

Analysis of the low- Ra regime in appendix A shows that with $\ell_x/h = 4$ the first variation of the Nusselt number away from unity is

$$Nu^{\text{FS}} = 1 + \left(\frac{Ra}{21\,567.5} \right)^2 + \text{ord}(Ra^4), \quad (3.3)$$

and

$$Nu^{\text{NS}} = 1 + \left(\frac{Ra}{87\,789.8} \right)^2 + \text{ord}(Ra^4). \quad (3.4)$$

The low- Ra regime means that the Ra^2 term in (3.3) and (3.4) is less than one, i.e., that the convective buoyancy transport is a weak enhancement of the diffusive transport. For **FS** low Ra means that Ra is somewhat less than about 10^4 and for **NS** low Ra means that Ra is somewhat

Ra	Free-slip Nu		No-slip Nu		Highest resolution n_x, n_z
	2D \circ	3D \bullet	2D \square	3D \blacksquare	
1.28e03	1.00	1.00 [†]	1.00	1.00 [†]	128, 32
3.20e03	1.02	1.02 [†]	1.00	1.00 [†]	128, 32
4.48e03	1.04	1.04 [†]	1.00	1.00 [†]	128, 32
6.40e03	1.08	1.08 [†]	1.01	1.01 [†]	128, 32
1.28e04	1.22	1.22 [†]	1.02	1.02 [†]	128, 32
1.92e04	1.38	1.38 [†]	1.04	1.04 [†]	128, 32
3.20e04	1.64	1.64 [†]	1.11	1.11 [†]	128, 32
6.40e04	2.07	2.07 [†]	1.28	1.28 [†]	128, 32
1.28e05	2.55	2.55 [†]	1.59	1.59 [†]	128, 32
2.56e05	3.04	3.04 [†]	1.96	1.96 [†]	128, 32
6.40e05	3.71	3.71 [†]	2.47	2.47 [†]	128, 32
1.60e06	4.50	4.50 [†]	3.01	3.01 [†]	256, 64
3.20e06	5.14	5.14 [†]	3.45	3.45 [†]	256, 64
6.40e06	5.80	5.80 [†]	3.93	3.93 [†]	256, 64
1.60e07	6.77	6.77 [†]	4.70	4.70 [†]	256, 64
3.20e07	7.61	7.61 [†]	5.38	5.44 [#]	256, 64
6.40e07	8.65	8.68*	6.17	6.59 [#]	256, 64
1.60e08	10.48	10.57*	7.41	8.46 [#]	256, 64
3.20e08	12.17*	12.19*	8.51	10.11 [#]	256, 64
6.40e08	14.01*	14.09*	9.69	11.97*	256, 64
1.60e09	16.99*	17.07*	11.77*	14.75*	256, 64
3.20e09	19.60*	20.32*	13.53*	17.20*	512, 128
6.40e09	22.41*	24.64*	15.35*	19.86*	512, 128
1.60e10	27.32*	31.38*	18.83*	23.67*	512, 128
3.20e10	31.48*	37.28*	21.88*	27.61*	512, 128
6.40e10	36.08*	43.94*	25.50*	30.68*	512, 128
1.28e11	41.85*	49.74*	29.87*	36.67*	1024, 256
1.60e11	43.80*		32.02*		1024, 256
3.20e11	50.71*	59.91*	37.45*	44.01*	1024, 256
6.40e11	58.36*		44.23*		1024, 256
1.60e12	71.43*		55.65*		1024, 256
3.20e12	86.26*		66.97*		2048, 512
6.40e12	101.32*		78.86*		4096, 1024
1.60e13	128.44*		97.66*		4096, 1024
6.40e13	178.55*		133.16*		4096, 1024

Table 1: Nu - Ra data for HC DNS. All runs have $Pr = 1$ and $\ell_x/h = 4$. 3D runs have $\ell_y/h = 1$ and $n_y = n_z$. The surface buoyancy is the sinusoid in (2.4). Unsteady solutions are indicated by a superscript * on Nu ; strictly 2D solutions (no y -dependence and $v = 0$) of 3D computations are marked by a superscript †. The four NS runs with superscript # are 3D but steady.

less than about 4×10^4 . These analytic results are compared with numerical solutions in the insert of figure 3. In table 1 all values of Nu are rounded to 2 decimal places, e.g., the 2DFS solution at $Ra = 6.4$ has $Nu - 1 = 8.8 \times 10^{-8}$ and at $Ra = 640$, $Nu - 1 = 8.8 \times 10^{-4}$. (These boring runs are not reported in table 1.)

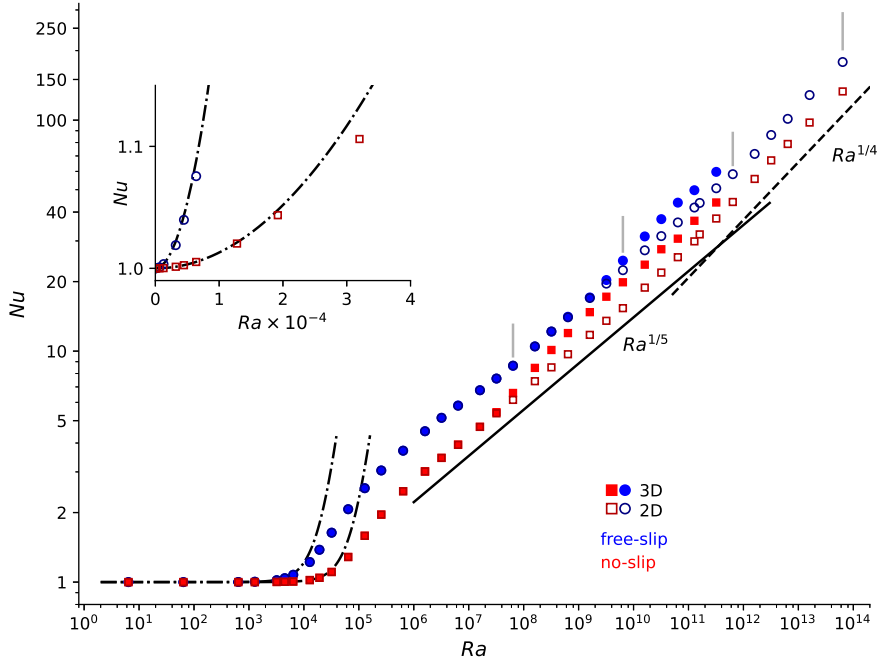


Figure 3: Variation of Nusselt number Nu with Rayleigh number Ra using the data from table 1. The inset compares the low- Ra numerical results with the low- Ra analytic results (3.3) and (3.4). Note that some solid markers fall on top of open markers, indicating that the 3D solutions evolve to become 2D, or that the three dimensionality is weak. The four vertical grey line segments mark Ra 's of the solutions in figures 1 and 2.

3.2. Nu - Ra scaling regimes: one-fifth and one-fourth

Between $Ra \sim 10^4$ and 10^5 we do not see a simple relation between Nu and Ra . But once Ra is greater than about 6.4×10^5 we find Rossby's scaling,

$$Nu \sim K_{1/5} Ra^{1/5}, \quad (3.5)$$

in all four solution suites. See section 4 for a discussion of Rossby's scaling argument, and for more recent arguments that also predict the exponent 1/5 in (3.5) (Gayen *et al.* 2014; Shishkina *et al.* 2016). Starting at around $Ra \sim 10^{11}$ in the 2DNS suite and 10^{12} in the 2DFS suite there is a transition from the one-fifth regime (3.5) to the one-fourth regime,

$$Nu \sim K_{1/4} Ra^{1/4}. \quad (3.6)$$

The one-fourth regime with NS has been documented previously by Tsai *et al.* (2020).

In figure 4 we show the data from figure 3, replotted using the compensated Nusselt number $Ra^{-1/5}Nu$ in panel (a) and $Ra^{-1/4}Nu$ in panel (b). Table 2 summarizes the exponents determined by least-squares fitting the Ra - Nu data over selected ranges. Least-squares exponents are broadly in agreement with the scaling regimes determined by visual inspection of figure 4 and other compensated plots. We use least-squares because it is objective and reproducible. Least squares also assesses the sensitivity of estimated exponents to the points at the beginning and end of a putative scaling range.

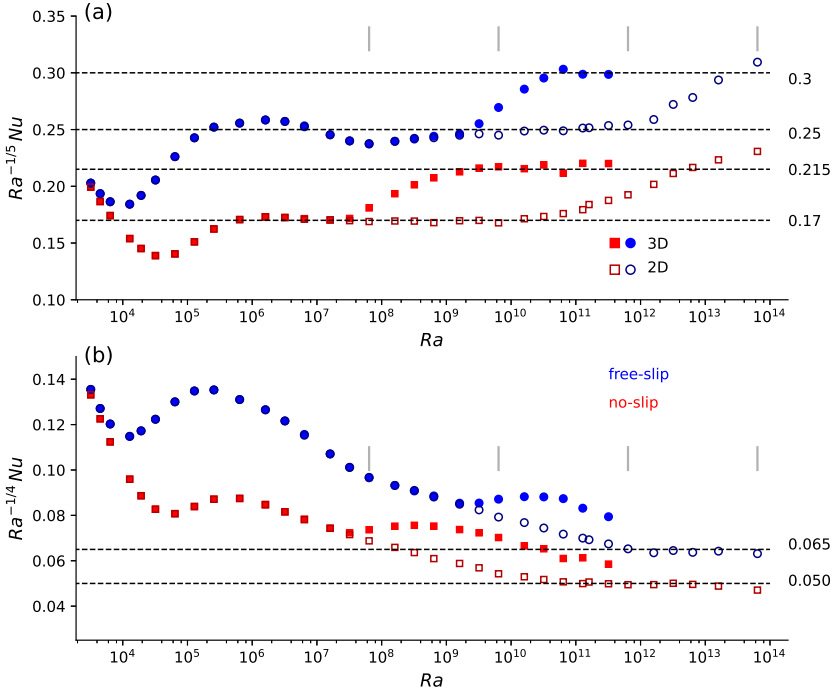


Figure 4: Variation of “compensated Nusselt numbers” (a) $Ra^{-1/5}Nu$ and (b) $Ra^{-1/4}Nu$ with Rayleigh number Ra . The four vertical grey line segments mark Ra ’s of the solutions in figures 1 and 2.

3.3. Discussion of the no-slip solutions

We begin with easiest case, which is the **2DNS** solution suite. The one-fifth scaling (3.5) is found across the four-decade range in row 1 of table 2; this is the plateau at $K_{1/5} = 0.17$ in figure 4(a). Least-squares estimates of exponent and prefactor, $K_{1/5}$, are robust to changes in the range, e.g., row 2 of table 2. The **2DNS** suite transitions to the one-fourth scaling (3.6) at around $Ra = 10^{11}$ and forms the plateau at $K_{1/4} = 0.05$ in figure 4(b); see rows 4 through 6 of table 2.

The **3DNS** solution suite is more complicated. With moderate Ra (rows 7 through 9 of table 2) the **3DNS** solutions coincide with their **2DNS** partners and the scaling is again (3.5) with $K_{1/5} = 0.17$. At a critical Ra , roughly 3.2×10^7 , the **3DNS** suite becomes unstable to 3D perturbations. With further increases in Ra the **3DNS** solutions have larger Nu than their **2DNS** colleagues: the four steady **3DNS** solutions in the interval $3.20 \times 10^7 \leq Ra \leq 3.20 \times 10^8$, are here. One might hope that development of 3D flow, albeit steady 3D flow, signals the beginning of a new scaling regime, with an exponent greater than one-fifth. But alas, this is the transition discovered by [Gayen et al. \(2014\)](#): at about $Ra = 1.60 \times 10^9$ the **3DNS** solutions enter a new one-fifth regime: see rows 10 through 12 of table 2 and the **3DNS** plateau at 0.215 in figure 4(a). With maximum $Ra = 3.20 \times 10^{11}$, we did not find convincing evidence of the one-fourth scaling (3.6) in the **3DNS** solution suite.

The **NS** computations of [Gayen et al. \(2014\)](#) used $Pr = 5$ and a piecewise constant surface

row	suite	range	points	least squares Nu
1	2DNS	$6.40 \times 10^5 \leq Ra \leq 6.40 \times 10^9$	13	$0.177 Ra^{0.198}$
2	2DNS	$1.60 \times 10^6 \leq Ra \leq 3.20 \times 10^9$	11	$0.178 Ra^{0.197}$
4	2DNS	$6.40 \times 10^{10} \leq Ra \leq 6.40 \times 10^{13}$	10	$0.062 Ra^{0.242}$
5	2DNS	$6.40 \times 10^{10} \leq Ra \leq 1.60 \times 10^{13}$	9	$0.056 Ra^{0.246}$
6	2DNS	$1.28 \times 10^{11} \leq Ra \leq 1.60 \times 10^{13}$	8	$0.055 Ra^{0.246}$
7	3DNS	$6.40 \times 10^5 \leq Ra \leq 3.20 \times 10^7$	6	$0.173 Ra^{0.199}$
8	3DNS	$6.40 \times 10^5 \leq Ra \leq 6.40 \times 10^6$	4	$0.167 Ra^{0.202}$
9	3DNS	$3.20 \times 10^6 \leq Ra \leq 3.20 \times 10^7$	4	$0.179 Ra^{0.197}$
10	3DNS	$1.60 \times 10^9 \leq Ra \leq 3.20 \times 10^{11}$	8	$0.195 Ra^{0.204}$
11	3DNS	$1.60 \times 10^9 \leq Ra \leq 1.60 \times 10^{10}$	4	$0.191 Ra^{0.205}$
12	3DNS	$3.20 \times 10^{10} \leq Ra \leq 3.20 \times 10^{11}$	4	$0.180 Ra^{0.208}$
20	2DFS	$6.40 \times 10^5 \leq Ra \leq 1.60 \times 10^{11}$	18	$0.253 Ra^{0.199}$
21	2DFS	$6.40 \times 10^5 \leq Ra \leq 3.20 \times 10^8$	9	$0.312 Ra^{0.186}$
22	2DFS	$6.40 \times 10^8 \leq Ra \leq 1.60 \times 10^{11}$	9	$0.215 Ra^{0.206}$
23	2DFS	$6.40 \times 10^{11} \leq Ra \leq 6.40 \times 10^{13}$	6	$0.074 Ra^{0.245}$
24	2DFS	$6.40 \times 10^{11} \leq Ra \leq 3.20 \times 10^{12}$	3	$0.082 Ra^{0.241}$
25	2DFS	$6.40 \times 10^{12} \leq Ra \leq 6.40 \times 10^{13}$	3	$0.073 Ra^{0.245}$
26	3DFS	$6.40 \times 10^5 \leq Ra \leq 3.20 \times 10^8$	9	$0.308 Ra^{0.187}$
27	3DFS	$6.40 \times 10^{10} \leq Ra \leq 3.20 \times 10^{11}$	3	$0.358 Ra^{0.193}$

Table 2: Summary of least-squares fits to various scaling regimes. Where possible, we assess the sensitivity of the exponent by varying the range.

buoyancy. Instead of (2.10), Gayen *et al.* (2014) defined Nu based on the buoyancy flux through the destabilized portion of the non-uniformly heated surface. Despite these differences, Gayen *et al.* (2014) document analogous 3DNS behavior within the one-fifth scaling regime: the constant $K_{1/5}$ takes different values on either side of a smooth transition.

3.4. Discussion of the free-slip solutions

Turning to the 2DFS solutions, the most generous identification of the one-fifth regime in (3.5) is the five-decade range in row 20 of table 2. These 18 points correspond to the plateau $K_{1/5} = 0.25$ in figure 4(a). We are concerned, however, by 9 points in the first half of this range, i.e., row 21 of table 2. These 9 points undulate around the $K_{1/5} = 0.25$ plateau with an amplitude of about ± 0.01 and the least-squares exponent 0.186 is uncomfortably different from $1/5$. These wayward points, at only moderately large Ra , correspond to solutions that are either steady, or weakly time dependent. Thus insufficient time-averaging in the estimate of Nu is not an issue. Moreover in this range the 2D and 3D solutions coincide. We conducted several tests by changing the spatial resolution and found no significant variation in the numerical estimate of Nu . If one views the exponent 0.186 as close to $1/5$ then the wayward points are the lower end of a five-decade 2DFS scaling regime: the undulation is a pre-asymptotic imperfection in the first half of this regime. A more cautious interpretation is that the 2DFS

one-fifth regime begins only at about $Ra = 6.40 \times 10^8$ and consists of the 9 points in row 22 of table 2. The 2DFS suite transitions to the one-fourth scaling (3.6) at around $Ra = 10^{12}$ and forms the plateau at $K_{1/4} = 0.065$ in figure 4(b); see rows 23 through 25 of table 2.

The 3DFS solutions depart significantly from their 2DFS colleagues first at about $Ra = 3.20 \times 10^9$. There is no evidence for a one-fourth scaling in the 3DFS suite. Instead, the three highest Ra 3DFS solutions (row 27 of table 2) indicate a second one-fifth regime e.g. the 0.3 plateau in figure 4(a). We speculate that the 3DFS suite is recapitulating the phenomenology seen in the 3DNS suite: two one-fifth scaling regimes separated by a smooth transition. We caution, however, that this speculation is based on three solutions in row 27 spanning less than one decade variation in Ra .

4. Review of $Nu \sim Ra^{1/5}$ scaling arguments

Rossby (1965) proposed a visco-diffusive balance in the boundary layer adjacent to the non-uniformly heated surface and so arrived at the one-fifth scaling in (3.5). Rossby identified the length scale

$$\delta_{1/5} \stackrel{\text{def}}{=} Ra^{-1/5} h \quad (4.1)$$

as the thickness of the surface BL. In the following discussion we also need the length

$$\delta_{1/4} \stackrel{\text{def}}{=} Ra^{-1/4} h. \quad (4.2)$$

At $Ra = 6.4 \times 10^{13}$, the ratio of these two BL scales is $\delta_{1/5}/\delta_{1/4} \approx 5$.

Central to Rossby's argument is the assumption that BL buoyancy forces are balanced by viscosity and that BL inertia is subdominant. At moderately large Ra , the exponent 1/5 has been supported by subsequent laboratory work and by numerical studies (Rossby 1998; Mullarney *et al.* 2004; Siggers *et al.* 2004; Wang & Huang 2005; Sheard & King 2011; Ilicak & Vallis 2012). With $Pr = \infty$, and with both no-slip and free-slip boundary conditions, Chiu-Webster *et al.* (2008) provide a compelling confirmation that $Nu \sim Ra^{1/5}$ as $Ra \rightarrow \infty$.

We emphasize that the scaling (3.5), and the associated BL thickness $\delta_{1/5}$, does not, however, require that $Pr \gg 1$. For example, the experiments of Mullarney *et al.* (2004) and Wang & Huang (2005) present evidence of Rossby scaling in unsteady flows. The 2D solutions shown in figure 1 – including the unsteady solution in panels (c) and (d) – are well within the $K_{1/5} = 0.25$ regime of figure 4(a). Our unsteady 2DFS solutions exhibit the one-fifth scaling (3.5) over at least three decades of Ra .

To further complicate the situation, 2D solutions in the one-fourth regime (3.6) still express the BL scale $\delta_{1/5}$: figure 5 shows a progressively expanded view of the structure of HC near the upper surface. This 2DNS solution is in the *non-Rossby* scaling regime (3.6). Nonetheless, panel (d) of figure 5 indicates that $\delta_{1/5}$ is a useful BL length scale. We conclude that at sufficiently high Ra there is a double BL: there is a thin- $\delta_{1/4}$ layer nested with a thicker $\delta_{1/5}$ -layer. We discuss this double BL further in section 5.

(The 2DNS solution in figure 5(a) exhibits the vortex-gas phenomenology noted previously in the 2DFS solutions shown in figure 2. At high Ra , no matter the viscous boundary condition, the interior of 2D HC is characterized as a vortex gas.)

As an alternative to Rossby scaling, Shishkina *et al.* (2016) proposed a set of scaling arguments summarized in a phase diagram of the (Ra, Pr) -plane. This diagram shows high- Pr regions denoted I_ℓ^* , I_∞ and III_∞ ; these three high- Pr regions have $Nu \sim Ra^\xi$ with exponent $\xi = 1/4$ in I_ℓ^* and III_∞ and $1/6$ in I_∞ . This tripartite proposal cannot be reconciled with the high- Pr results of Rossby (1965) and Chiu-Webster *et al.* (2008). Instead, in the phase diagram of Shishkina *et al.* (2016), the one-fifth scaling (3.5) is found only in the *low-Pr* region I_ℓ . We discuss the Shishkina *et al.* (2016) I_ℓ regime in more detail below.

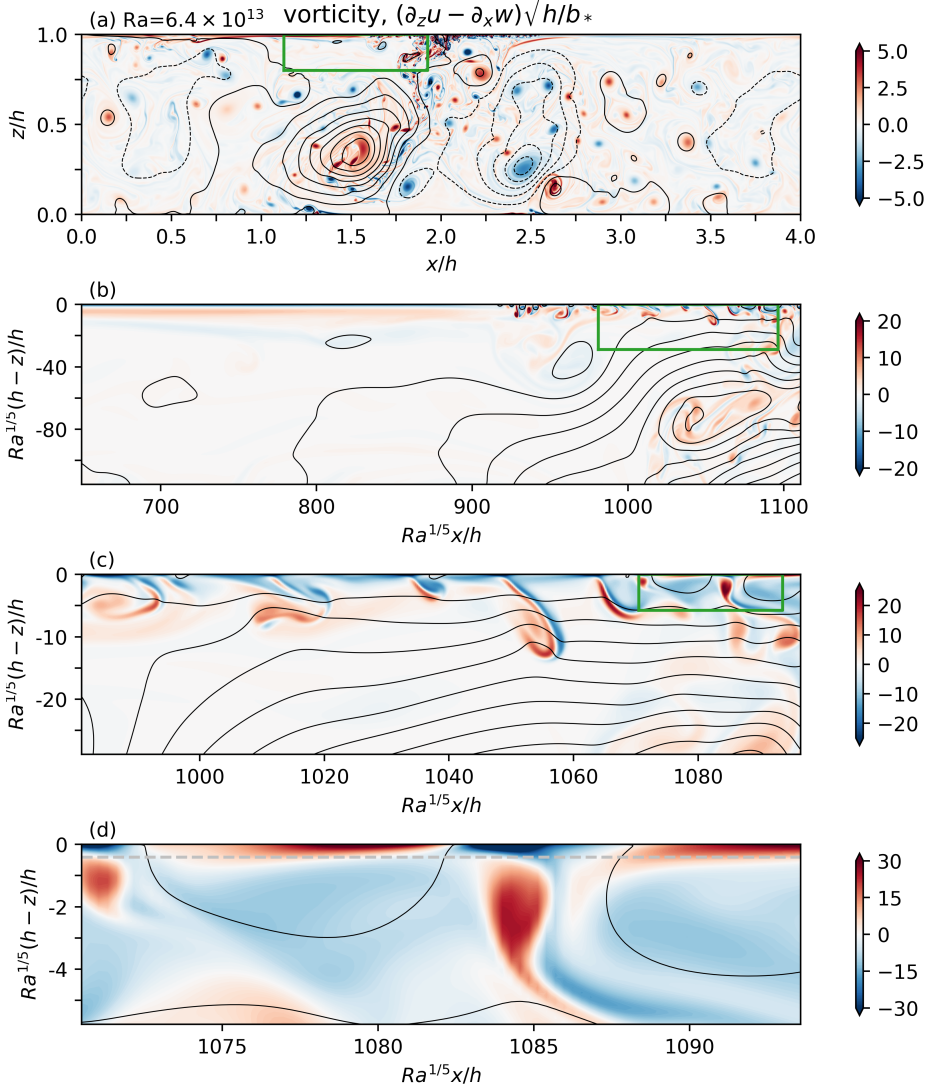


Figure 5: (a) A snapshot of vorticity in the 2DNS solution at $\text{Ra} = 6.4 \times 10^{13}$; this solution is in the non-Rossby $Nu \sim \text{Ra}^{1/4}$ scaling regime. Panels (b)-(d) depict the boundary-layer structure by progressively zooming in to the top surface. Green rectangles in panels (a), (b) and (c) indicate the regions in panels (b), (c) and (d) respectively. In panels (b), (c) and (d), both axes are measured in units of $\delta_{1/5}$. The dashed grey line in panel (d) indicates the distance $2\delta_{1/4}$ below the top surface $z = h$. The contours in all panels are streamlines.

4.1. The spanwise average

To identify the various processes in the BL, we begin taking a spanwise y -average of the equations of motion. Denote this spanwise average with a hat so that

$$b(x, y, z, t) = \underbrace{\frac{1}{\ell_y} \int_0^{\ell_y} b(x, y, z, t) \, dy}_{\stackrel{\text{def}}{=} \hat{b}(x, z, t)} + b'(x, y, z, t). \quad (4.3)$$

Above, $b'(x, y, z, t)$ is the three-dimensional departure from the spanwise average. Taking the spanwise average of the 3D continuity equation (2.3), we obtain a 2D “overturning stream function” $\psi(x, z, t)$, such that $(\hat{u}, \hat{w}) = (-\psi_z, \psi_x)$. With this notation the 3D velocity is written as

$$(u, v, w) = (-\psi_z, 0, \psi_x) + (u', v', w') . \quad (4.4)$$

The spanwise-average of the buoyancy equation is

$$\hat{b}_t + \psi_x \hat{b}_z - \psi_z \hat{b}_x + \partial_x \widehat{u' b'} + \partial_z \widehat{w' b'} = \kappa \nabla^2 \hat{b} , \quad (4.5)$$

and the spanwise average of the spanwise vorticity equation is

$$\underbrace{\zeta_t + \psi_x \zeta_z - \psi_z \zeta_x}_{\text{inertia}} + \underbrace{\hat{b}_x}_{\text{buoyancy torque}} + \underbrace{(\partial_z^2 - \partial_x^2) \widehat{u' w'} + \partial_x \partial_z (\widehat{u'^2} - \widehat{w'^2})}_{\text{Reynolds stress torque}} = \underbrace{\nu \nabla^2 \zeta}_{\text{viscosity}} , \quad (4.6)$$

where $\zeta \stackrel{\text{def}}{=} -\nabla^2 \psi$ is the spanwise-averaged spanwise vorticity. The power integral (2.8) becomes

$$\varepsilon = \nu \langle \zeta^2 \rangle + \nu \langle |\nabla \mathbf{u}'|^2 \rangle \quad (4.7)$$

$$= -\kappa \bar{b}(0)/h . \quad (4.8)$$

The 2D equations of motion are recovered by suppressing the spanwise averages of quadratic fluctuations in (4.5), (4.6), and (4.7).

4.2. A review of $Nu \sim Ra^{1/5}$ scaling arguments

Following Shishkina *et al.* (2016), we assume that there is a BL with thickness δ_b in buoyancy and δ_u in momentum and vorticity. The Reynolds number is

$$Re \stackrel{\text{def}}{=} \frac{U h}{\nu} , \quad (4.9)$$

where

$$U \stackrel{\text{def}}{=} \sqrt{\langle |\mathbf{u}|^2 \rangle} \quad (4.10)$$

is the typical flow velocity. We use the depth h as representative of the domain dimensions, i.e., $(\ell_x, \ell_y) \sim h$; these three length scales are roughly comparable.

Scale analysis of the surface Nusselt number in (2.11), e.g., $\hat{b}_z(h) \sim b_\star/\delta_b$, shows that

$$Nu \sim \frac{h}{\delta_b} . \quad (4.11)$$

One reaches the same conclusion via scale analysis of the χ -based Nusselt number in (2.9): although $|\nabla b|^2 \sim b_\star^2/\delta_b^2$, the χ -BL occupies only a fraction δ_b/h of the domain. Thus (4.11) follows because of the volume average $\langle \cdot \rangle$.

Now apply scale analysis to the buoyancy equation (4.5). Using results such as $\psi_z \hat{b}_x \sim \psi_x \hat{b}_z \sim U b_\star/h$ and $\kappa \nabla^2 \hat{b} \sim \kappa b_\star/\delta_b^2$ one has

$$U \sim \frac{\kappa h}{\delta_b^2} , \quad \text{or in non-dimensional form} \quad Nu \sim (Re Pr)^{1/2} . \quad (4.12)$$

To estimate the viscous dissipation ε on the right of the power integral (4.7), one assumes that an order-one fraction of ε is concentrated in the BL, and this BL occupies a fraction δ_u/h of the domain. One can either neglect $\nu \langle |\nabla \mathbf{u}'|^2 \rangle$, or assume that both terms on the right

of (4.7) scale in the same way, i.e., as $\nu\zeta^2 \sim \nu(U/\delta_u)^2$. In either case

$$\varepsilon \sim \frac{\nu U^2}{\delta_u h}. \quad (4.13)$$

Scale analysis of the right of (4.8) assumes that the bottom buoyancy, $\bar{b}(0)$, is an order-one fraction of the minimum buoyancy, $-b_\star$, on the top surface. (The stronger result that $\bar{b}(0) \rightarrow -b_\star$ as $Ra \rightarrow \infty$ is likely true.) Thus

$$\varepsilon \sim \frac{\kappa b_\star}{h}. \quad (4.14)$$

Combining (4.13) and (4.14)

$$U^2 \sim \frac{\kappa}{\nu} \delta_u b_\star, \quad \text{or in non-dimensional form} \quad (RePr)^2 \sim \frac{\delta_u}{h} Ra. \quad (4.15)$$

Eliminating $RePr$ between (4.12) and (4.15), and then using (4.11) to get rid of h , one finds

$$Nu^5 \sim \frac{\delta_u}{\delta_b} Ra. \quad (4.16)$$

The final step to obtain the dependence of Nu on Ra and Pr is to express the ratio δ_u/δ_b on the right of (4.16) in terms Ra and Pr . There are three arguments in the literature.

The scaling of Rossby (1965). Taking $\delta_u = \delta_b$ one obtains from (4.16)

$$Nu \sim Pr^0 Ra^{1/5} \quad \text{and} \quad Re \sim Pr^{-1} Ra^{2/5}. \quad (4.17)$$

Rossby's 1965 argument did not employ the power integral and its consequence (4.16). Instead, Rossby assumes *ab initio* that $\delta_b = \delta_u$ and balances buoyancy torque with viscosity in (4.6), leading to $U \sim b_\star \delta_u^3 / \ell \nu$. Combining these results with (4.11) and (4.12) one again finds (4.17). Rossby's balance between buoyancy torque and viscosity applies to both **FS** and **NS**. In the **FS** case, the velocity BL results from the vorticity source \hat{b}_x in (4.6): this rationalization of Rossby's assumption that $\delta_u = \delta_b$ also applies to **NS**.

The scaling of Gayen, Griffith & Hughes (2014). In the vorticity equation (4.6), balance buoyancy torque with either inertia or Reynolds stress torques, leading to $U^2 \sim \delta_u b_\star$, and follow Rossby by assuming that $\delta_b = \delta_u$. Combining these results with (4.11) and (4.12) one finds

$$Nu \sim Pr^{1/5} Ra^{1/5} \quad \text{and} \quad Re \sim Pr^{-3/5} Ra^{2/5}. \quad (4.18)$$

This argument does not use the power integral and it is not consistent with (4.16) unless Pr is order unity. Using the scaling assumptions above to estimate ε in (4.7) and (4.8) we find

$$\nu \langle \zeta^2 \rangle \sim Ra (\kappa \nu^2 / h^4) \quad \text{and} \quad -\kappa \bar{b}(0)/h \sim Ra (\kappa^2 \nu / h^4). \quad (4.19)$$

The two terms in (4.19) differ by a factor of Pr : this is a problem if Pr is either very large or very small. But with Pr of order unity – and here we consider $Pr = 1$ – there is no problem closing the mechanical energy budget and thus the scaling of **Gayen et al. (2014)** is a valid alternative to that of Rossby.

The scaling of Shishkina, Grossman & Lohse (2016). In the vorticity equation (4.6), balance inertia with viscosity, leading to $U \sim \nu h / \delta_u^2$. Eliminating U with (4.12) one finds $\delta_u = Pr^{1/2} \delta_b$, and substituting into the power-integral (4.16)

$$Nu \sim Pr^{1/10} Ra^{1/5}, \quad \text{and} \quad Re \sim Pr^{-4/5} Ra^{2/5}. \quad (4.20)$$

A distinctive feature of this scaling argument is that buoyancy torque \hat{b}_x in (4.6) does not appear in the leading-order BL vorticity balance. This is justified by requiring that $Pr \ll 1$, so

that $\delta_u = Pr^{1/2} \delta_b \ll \delta_b$. In other words, this visco-inertial BL is so thin that both viscosity and inertia are much greater than the buoyancy torque $\hat{b}_x \sim b_\star/h$.

Despite different physical assumptions, the three arguments summarized above are in agreement that $Nu \sim Ra^{1/5}$: all differences lie in the dependence of Nu on Pr . In this respect scaling (4.20) – corresponding to region I_ℓ in the phase diagram of Shishkina *et al.* (2016) – needs clarification. Region I_ℓ , with $Pr \ll 1$, is referred to by Shishkina *et al.* (2016) as “Rossby scaling”. Although the exponent one-fifth is the same as that of Rossby, the dependence on Pr in (4.20) differs from that of Rossby in (4.17). Moreover Rossby was concerned with $Pr \gg 1$, while scaling (4.20) ostensibly applies provided that $Pr \ll 1$. Thus referring to I_ℓ as Rossby scaling is a misnomer: the phase diagram does not contain a region corresponding to the original Rossby scaling in (4.17).

5. Nested boundary layers and the $Nu \sim Ra^{1/4}$ scaling

Tsai *et al.* (2020) investigate 2DNS HC with $Pr = 6.14$. With $Ra > 10^{10}$, and provided that the imposed surface buoyancy varies linearly with the horizontal coordinate x , Tsai *et al.* (2020) report the one-fourth scaling (3.6) extending over four decades of Ra . Here, using the sinusoidal surface buoyancy (2.4), we also find the one-fourth scaling (3.6) in the 2DFS and 2DNS solution suites. Tsai *et al.* (2020) speculate that their one-fourth scaling might correspond to a regime proposed by Shishkina *et al.* (2016) in their phase diagram of the (Ra, Pr) parameter plane. In this scheme the (Ra, Pr) -plane is partitioned into seven regions and the exponent 1/4 is located in regions III_∞ , IV_u , and I_ℓ^* . But we now show that defining features of III_∞ , IV_u , and I_ℓ^* do not agree with the numerical solutions. We conclude that the exponent one-fourth found here, and likely in the regime identified by Tsai *et al.* (2020), is *not* in agreement with any region of the phase diagram of Shishkina *et al.* (2016).

5.1. Partitioning of buoyancy dissipation χ between BL and interior

A main characteristic distinguishing the various regimes by Shishkina *et al.* (2016) is the partitioning of kinetic energy dissipation, ε , and buoyancy variance dissipation, χ , between the BL and the interior of the domain. To quantify the partitioning of χ we introduce the function

$$F_\chi(z) \stackrel{\text{def}}{=} \frac{\kappa}{h} \int_0^z \overline{|\nabla b|^2} dz' / \chi, \quad (5.1)$$

where the overbar denotes an (x, y, t) -average; see figure 6. $F_\chi(z)$ increases monotonically from 0 to 1 with z/h and indicates the fraction of buoyancy-variance dissipation below the level z . In the 2DFS case, figure 6(a) shows that χ is increasingly localized within a BL as $Ra \rightarrow \infty$. Examination of $F_\chi(z)$ for the 2DNS solutions indicates no significant differences from the 2DFS results in figure 6(a). With both FS and NS, χ is increasingly concentrated within a BL as $Ra \rightarrow \infty$.

A main characteristic of regions III_∞ and IV_u in the phase diagram of Shishkina *et al.* (2016) is that χ is dominantly in the interior of the domain. Thus figure 6(a) disqualifies regions III_∞ and IV_u . The remaining possibility with exponent 1/4 is the $Pr \gg 1$ region I_ℓ^* , characterized by a momentum BL that is much thicker than the buoyancy diffusion BL. But region I_ℓ^* is located at moderate values of Ra in the phase diagram so that 1/4 is the first exponent encountered if Pr is fixed and Ra is increased from small values. In our 2D solutions, however, we first find the 1/5 scaling (3.5), which is replaced at higher Ra by 1/4 in (3.6). This is also the case in the study of Tsai *et al.* (2020): first 1/5 and then, at higher Ra , 1/4. We conclude that the exponent 1/4 in the 2D solution suites is not related to regions

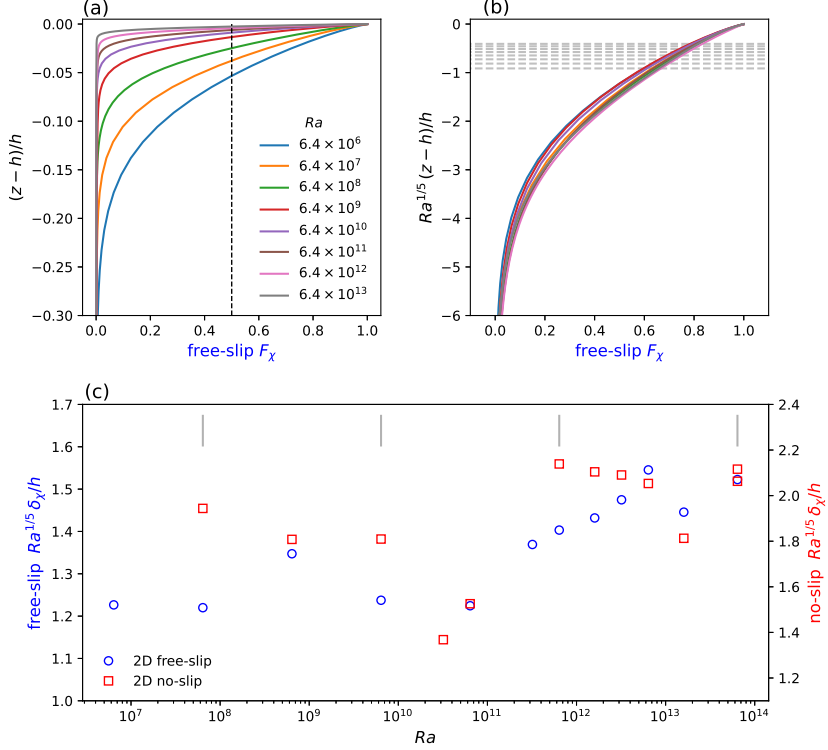


Figure 6: (a) The function $F_\chi(z)$ defined in (5.1) for the 2DFS solutions. The vertical axis is distance from the top surface at $z = h$. A BL thickness, δ_χ , is defined as the distance from the top at which $F_\chi(z) = 1/2$ (dashed vertical line in panel (a)). (b) Same as (a) but with the vertical axis rescaled with $Ra^{1/5}$. Horizontal grey dashed lines indicate the distance $2\delta_{1/4}$ below the top surface $z = h$. (c) The compensated BL thickness, $Ra^{1/5}\delta_\chi/h$, as a function of Ra . The four vertical grey line segments mark Ra 's of the solutions in figures 1 and 2.

III_∞ , IV_u and I_ℓ^* of the phase diagram. In section 6 we seek an alternative explanation for the one-fourth scaling regimes in figure 4(b).

To extract more information from $F_\chi(z)$, we scale the z -axis with $\delta_{1/5}$ and re-plot the results from figure 6(a) in figure 6(b): the curves now fall largely on top of each other, indicating that the function $F_\chi(z)$ expresses the BL thickness $\delta_{1/5}$, even if the $Nu \sim Ra^{1/4}$. To quantify this, we define a BL thickness, δ_χ , by determining the level at which $F_\chi(z) = 1/2$: see the dashed vertical line in figure 6(a). The compensated plot in figure 6(c) then shows that

$$\delta_\chi \approx K_\chi \delta_{1/5}. \quad (5.2)$$

The constant K_χ in (5.2) is about 1.5 for the FS solutions and 1.8 for the NS solutions.

The $Ra^{-1/5}$ scaling in (5.2) applies in *both* the one-fifth regime (3.5) and the one-fourth regime (3.6). Yet the reasoning in section 4, leading to

$$Nu \sim \frac{h}{\delta_b}, \quad (5.3)$$

underpins all scaling arguments and seems inescapable. It must be that in the one-fourth regime (3.6), the buoyancy BL has a double-layer structure: there is a thin BL, with thickness $\delta_b = \delta_{1/4}$, embedded within the thicker δ_χ -BL in (5.2).

(The scatter of K_χ in figure 6(c) might be considered uncomfortably large. Note, however,

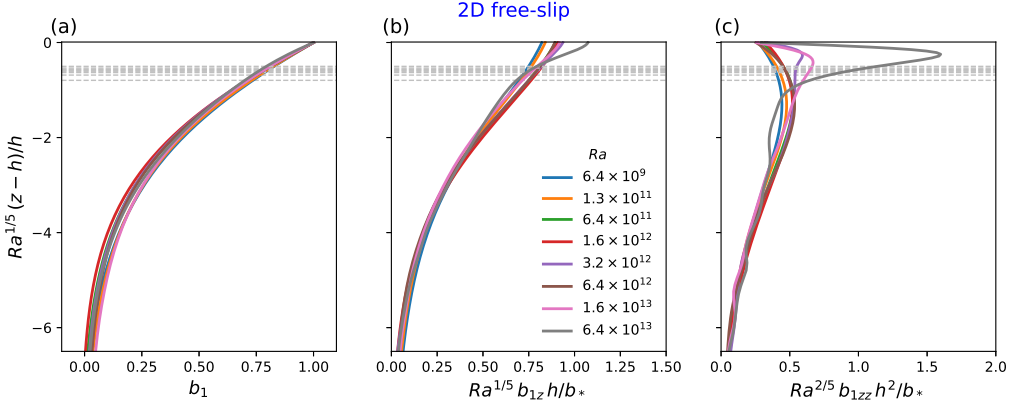


Figure 7: The structures of (a) $b_1(z)$, (b) $b'_1(z)$, and (c) $b''_1(z)$ for 2DFS solutions at various Ra . Note that $b_1(z)$ was obtained here just from the final snapshot of each simulation without any time-averaging. The vertical axis is distance from the surface $z = h$ measured in units of $\delta_{1/5}$. Horizontal grey dashed lines indicate the distance $2\delta_{1/4}$ below the surface.

that Ra is varied by seven decades. This large range encompasses the transition from steady to strongly time-dependent 2D flows. At $Ra = 6.4 \times 10^{13}$, $Ra^{-1/4}$ is smaller than $Ra^{-1/5}$ by a factor of 5, which is much greater than the $\pm 20\%$ scatter in figure 6(c).)

5.2. The $\delta_{1/4}$ -boundary layer

To identify the $\delta_{1/4}$ -BL in our solutions, and show consistency with (5.3) in the one-fourth regime, we notice that with the sinusoidal surface buoyancy in (2.4), the surface Nusselt number (2.11) is

$$Nu_s = b'_1(h) / b'_{\text{diff}}(h), \quad (5.4)$$

where above the prime denotes a z -derivative and

$$b_1(z) \stackrel{\text{def}}{=} 2 \overline{\cos kx b(x, y, z, t)}. \quad (5.5)$$

We define the thickness, δ_s , of this surface BL in (5.4) by

$$\delta_s \stackrel{\text{def}}{=} b_\star / b'_1(h), \quad (5.6)$$

where b_\star is the amplitude of the sinusoidal surface buoyancy in (2.4). The numerator in (5.6) is appropriate since $b_\star = b_1(h) = b_{\text{diff}}(h)$.

Figure 7 shows $b_1(z)$, and the first two derivatives of this averaged field. The overline in (5.5) indicates both a horizontal and temporal average. Unfortunately we did not collect a time series of b_1 and thus figure 7 is based on the horizontal average of single snapshots of the buoyancy field at the final time. The inner BL, with thickness $\delta_{1/4}$, is not visible in $b_1(z)$ in figure 7(a). But the higher derivatives of $b_1(z)$ in the panels (b) and (c) reveal the scale $\delta_{1/4}$ in the solution. In particular, the one-fourth scaling (3.6) results from the increase in $b'_1(h)$, evident in figure 7(b) as Ra increases. The maximum of $b''_1(z)$ in figure 7(c) appears only in the one-fourth regime (3.6).

Figure 8(a) shows δ_s , diagnosed from (5.6), and compensated by $Ra^{-1/5}$. In the one-fifth scaling regime (3.5), with Ra less than about 10^{11} , $Ra^{-1/5} \delta_s / h$ varies between about 2.6 and 2.9. In these cases both δ_s and δ_χ are $\sim \delta_{1/5}$. Figure 8(b) shows that at the four or five highest values of Ra , $Ra^{-1/4} \delta_s / h$ varies between about 10.5 and 11.4. We conclude that in these

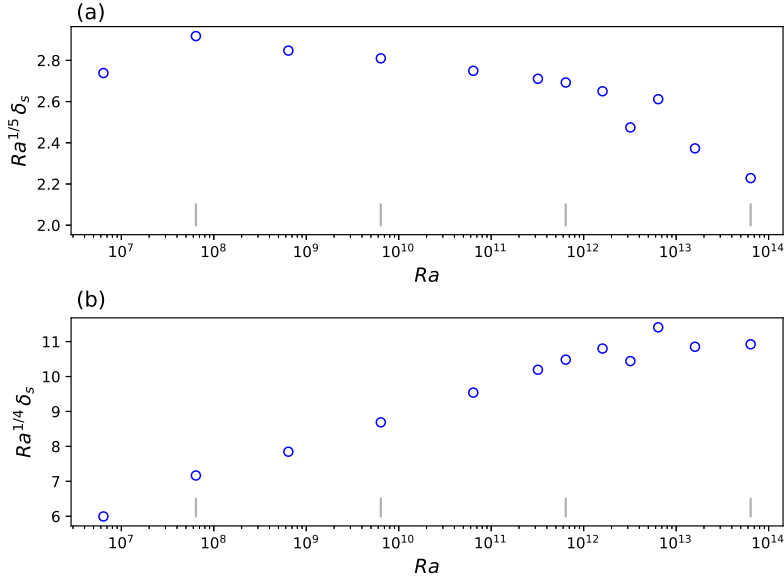


Figure 8: The compensated surface BL thickness, δ_s in (5.6), for the 2DFS suite. In (a) δ_s is compensated by $Ra^{-1/5}$ and in (b) by $Ra^{-1/4}$. The transition between the one-fifth scaling (3.5) and the one-fourth scaling (3.6) is at about 6.4×10^{11} . Vertical grey line segments mark the Ra values corresponding to the solutions in figures 1 and 2. Vertical grey line segments mark the Ra values corresponding to the solutions in figures 1 and 2.

cases $\delta_s \sim \delta_{1/4}$, but $\delta_\chi \sim \delta_{1/5}$. Via (5.3), the Nusselt number is determined by the $\delta_{1/4}$ inner BL, resulting in the one-fourth regime (3.6).

6. A scaling argument for $Nu \sim Ra^{1/4}$

In this section we present a scaling argument applicable to the one-fourth regime of horizontal convection. Although our numerical solutions revealed the one-fourth scaling regime only in the 2D cases, we still hold hope that the one-fourth regime might also emerge in 3D at sufficiently high Ra . With the 3D case in mind, we propose an overarching explanation for the one-fourth scaling – independent of boundary conditions, dimensionality and 2D vortex-gas phenomenology.

The one-fourth regime requires an inner buoyancy BL with thickness $\delta_b \sim \delta_{1/4}$. In discussing this inner BL it is helpful to keep figure 5(d) in mind: the $\delta_{1/4}$ -BL is identified by the dashed grey line. Think of this inner BL as a laminar sub-layer, stirred by the outer flow in the much thicker $\delta_{1/5}$ -BL. The overarching explanation alluded to above is that the thickness of the laminar sub-layer is related to the Kolmogorov and Batchelor length scales

$$\eta_K = \left(\frac{\nu^3}{\varepsilon} \right)^{1/4} \quad \text{and} \quad \eta_B = \left(\frac{\kappa^2 \nu}{\varepsilon} \right)^{1/4}. \quad (6.1)$$

These length scales are identified as the smallest scales of fluctuations in momentum and buoyancy that can survive before the damping by viscosity ν and diffusion κ is overwhelming. By analogy, the HC laminar sub-layer with thickness δ_b , is the thinnest BL that can survive in a horizontal-convective flow that is supplied with kinetic energy at a rate ε .

(In the arguments of Kolmogorov and Batchelor the viscous dissipation rate ε is also the energy cascade rate in a 3D inertial range. This interpretation of ε cannot apply to 2D HC: there is no vortex stretching in a 2D flow and therefore no forward cascade of energy. We argue instead that the laminar sub-layer thickness is determined by ε as the most basic measure of forcing strength and by the molecular parameters ν and κ . Thus $\delta_b \sim (\nu^p \kappa^q / \varepsilon)^{1/4}$, with $p + q = 3$, is dimensionally acceptable; η_K and η_B are the most prominent members of this family. Saying more would require varying Pr which is beyond our scope here.)

Following the scaling arguments reviewed section 4, we assume that $\bar{b}(0) \approx -b_\star$. Then, once again, the energy power integral (2.8) implies that

$$\varepsilon \sim \frac{\kappa b_\star}{h}. \quad (6.2)$$

With ε in (6.2), η_K and η_B in (6.1) can be written as

$$\frac{\eta_K}{h} = Pr^{1/2} Ra^{-1/4} \quad \text{and} \quad \frac{\eta_B}{h} = Pr^0 Ra^{-1/4}. \quad (6.3)$$

Thus if the laminar sub-layer has thickness $\delta_b \sim \eta_K$, or perhaps $\delta_b \sim \eta_B$, then $Nu \sim Ra^{1/4}$.

7. Discussion: is 3D horizontal convection turbulent?

Paparella & Young (2002) showed that as a consequence of the mechanical energy power integral (6.2), HC does not satisfy the zeroth law of turbulence. Paparella & Young also noted that the zeroth law is not a universally accepted as part of a definition of turbulence. For example, Scotti & White (2011) argued that the zeroth law is irrelevant because “HC can transport very large quantities of heat and sustain large amounts of diapycnal mixing with a surprisingly small amount of dissipation”. Similar sentiments, reinforced by arguments involving exchange between available potential energy and kinetic energy, are expressed by Gayen *et al.* (2013, 2014).

(Note that even the very form of zeroth law of turbulence appropriate to HC is also controversial. Paparella & Young (2002) state that ε should be non-zero as $(\nu, \kappa) \rightarrow (0, 0)$ with $Pr = \nu/\kappa$ fixed. In their “clarification” of the zeroth law, Shishkina *et al.* (2016) prefer a different limit in which $\nu \rightarrow 0$ with κ fixed. In this case, by inspection of (2.8), the zeroth law applies in the high-inertial limit in which $Ra \rightarrow \infty$ and simultaneously $Pr \rightarrow 0$.)

A common response to the question “What is turbulence?” (for example given by Google or by chatbot ChatGPT), is that “Turbulence is a fluctuation or disturbance in a fluid (such as air or water) that is characterized by chaotic and irregular movements.” However, there is more to turbulence than this, else the 2D solutions in figure 2 are turbulent. In addition to “chaotic and irregular movements” a transition to 3D flow is viewed as essential (Gayen *et al.* 2014; Tsai *et al.* 2016, 2020). It is only in 3D that “the high average vorticity which is known to exist in turbulent motion” can be produced by “extension of vortex filaments in an eddying fluid” (Taylor 1938).

In this section we use the four solution suites from section 3 to revisit the question of whether HC is “turbulent”. We show that the 3D solutions, with maximum $Ra = 3.2 \times 10^{11}$, cannot be considered turbulent. We also present theoretical arguments indicating that 3D HC cannot become turbulent at any Ra . We set aside the zeroth law of turbulence and focus instead on accepted characteristics of 3D hydrodynamic turbulence:

- (a) chaotic, disordered and irregular fluid motions, irreproducible in detail;
- (b) greatly enhanced transport of momentum and heat;
- (c) strong vorticity amplification by strain mediated 3D vortex stretching;
- (d) a direct cascade of energy in an inertial range;

(e) termination of the inertial range at the viscous length scale η_K .

According to Stewart in the educational film “Turbulence” (NCFMF 1968, 1972) these phenomena “give a defining syndrome, or set of symptoms, for turbulence”. (Stewart listed (a), (b), and (c); here we have added (d) and (e)).

Chaotic and disordered flow described by symptom (a) applies to both 2D and 3D time-dependent solutions at moderately high Ra , e.g., beyond 10^9 . Just based on symptom (a) one would conclude that 2D HC is turbulent. But because of symptoms (c) and (d), a 2D flow – no matter how erratically time dependent the velocity – cannot be turbulent (Taylor & Green 1937).

The 2D and 3D HC solutions coincide up to a critical Ra at which 3D instabilities first appear (Gayen *et al.* 2014; Tsai *et al.* 2016; Passaggia *et al.* 2017). This bifurcation to 3D flow is usually viewed as the first step in a transition to turbulence. But the unstable non-turbulent 2D solution is always present and serves as a “comparison flow” for putatively turbulent 3D solutions at the same Ra , and with the same boundary conditions. The main thrust of the argument that follows is that 3D HC is neither qualitatively nor quantitatively different from the non-turbulent 2D comparison flow: the onset of three-dimensionality in HC does not inflame turbulence symptoms (b) through (e).

A question of interest, especially in oceanographic context, is how much might HC contribute to total heat flux? Thus, how much can Nu be enhanced in turbulent HC has been a motivation for HC research. Symptom (b), emphasized by Scotti & White (2011) and other authors, demands that HC turbulence is accompanied by a large increase in the horizontal transport of heat. But in figure 3 and table 1, the 3D Nu is only 20% greater than that of the non-turbulent 2D comparison flow. Symptom (b) demands much more than a 20% enhancement in Nu between a turbulent 3D flow and a non-turbulent 2D comparison flow.

Moreover figure 3 and table 1 show that the viscous boundary condition (FS versus NS) has a larger quantitative effect on Nu than does dimensionality: even after the transition to unsteady 3D flow ($Ra \geq 6.4 \times 10^8$), the 3DNS solutions transport less buoyancy than the non-turbulent 2DFS solutions at the same Ra . If 3DNS transitions to turbulence at some $Ra > 3.2 \times 10^{11}$ then, no matter the boundary condition, the turbulent 3D flow should transport more heat than the non-turbulent 2D flow. There is no indication of this hypothetical crossover between 3DNS and 2DFS in figure 3.

Table 3 summarizes gross measures of the departures from the 2D spanwise-averaged circulation defined in (4.3). For both 3DNS and 3DFS, about two-thirds of the kinetic energy is in the spanwise averaged flow. In the third column the component of buoyancy gradient in the spanwise direction (b_y) contributes less than 2% to the buoyancy dissipation χ . The only statistic that is dominated by departures from the spanwise average is mechanical energy dissipation, ε , in the fourth column. Thus table 3, and particularly the third column, supports the view that the 3D Nu , even at $Ra = 3.20 \times 10^{11}$, is largely determined by the 2D spanwise averaged circulation, rather than by robust 3D turbulence characterized by (b) through (e). Figure 9(a) shows that there is no inertial cascade in the interior, i.e., (c) through (e) do not apply to this 3DFS solution (nor to the 3DNS solution). An inertial cascade is characterized by a kinetic energy spectrum $\sim \varepsilon^{2/3} k^{-5/3}$, or a vorticity spectrum $\sim \varepsilon^{2/3} k^{+1/3}$. The ultra-violet vorticity divergence is cut-off at a wavenumber of order η_K^{-1} . But in contradiction to (e) the snapshot in figure 9(a) shows that vorticity is concentrated on length scales very much larger than η_K .

We do not have an estimate of the length scale of the vorticity fluctuations in figure 9 (nor for the core radius of the 2D vortices in figure 2). These vorticity length scales are rather less than the domain scales (ℓ_x, ℓ_y, h), but very much greater than η_K in (6.3). There is, however, a simple result for the magnitude of the vorticity $\omega = \nabla \times \mathbf{u}$. With a well known identity, the kinetic energy dissipation can be written as $\varepsilon = \nu \langle |\omega|^2 \rangle$ and the mechanical

	$\langle \hat{\mathbf{u}} ^2 \rangle / \langle \mathbf{u} ^2 \rangle$	$\langle v^2 \rangle / \langle \mathbf{u} ^2 \rangle$	$\kappa \langle b_y^2 \rangle / \chi$	$\nu \langle \zeta^2 \rangle / \varepsilon$
3DFS	0.662	0.112	0.013	0.187
3DNS	0.690	0.092	0.019	0.342

Table 3: Statistics for the 3D solutions at $Ra = 3.20 \times 10^{11}$. The ratios above were computed from a single snapshot at the final time, i.e., without the benefit of time averaging. These ratios decrease monotonically to zero as Ra is lowered to the critical value for the onset of 3D motion. In the first column, $\hat{\mathbf{u}} = (-\psi_z, 0, \psi_x)$ is the spanwise averaged velocity in (4.4) and in the final column $\zeta = -\nabla^2 \psi$ is the vorticity of the spanwise-averaged flow.

power integral (2.8) rewritten as

$$\frac{\langle |\omega|^2 \rangle}{b_\star/h} = -\frac{\kappa}{\nu} \frac{\bar{b}(0)}{b_\star}, \quad (7.1)$$

$$\leq \frac{\kappa}{\nu}. \quad (7.2)$$

In passing from the exact equality (7.1) to the rigorous inequality in (7.2) we have used the extremum principle for buoyancy.

What is the significance of the bound (7.2)? It is remarkable that (7.2) is independent of aspect ratio ℓ_y/h . Thus at high Ra , with $\bar{b}(0)$ close to $-b_\star$, 3D HC must have almost the same $\langle |\omega|^2 \rangle$ as that of the non-turbulent 2D comparison flow. Near equality of $\langle |\omega|^2 \rangle$ in 2D and 3D is incompatible with turbulence vorticity amplification symptom (c). We can safely deduce that even a wider domain (increasing ℓ_y/h) would not produce a large increase in Nu resulting from turbulent transport. Moreover, if the Kolmogorov and Batchelor length scales in (6.3) control the thickness of the transport-determining BL then indeed ℓ_y/h is irrelevant.

To reinforce and illustrate the conclusion above, note that $\bar{b}(0)$ of the $Ra = 6.4 \times 10^{13}$ 2D solution in figure 2(d) is within 15% of the minimum $-b_\star$. Thus the root-mean-square (RMS) vorticity of this 2D flow is within 8% of the maximum $\sqrt{b_\star/h}$ implied by (7.2). (In this example $\kappa/\nu = 1$.) It follows that a 3DFS HC solution at $Ra = 6.4 \times 10^{13}$, and $Pr = 1$, must have an RMS vorticity within 8% of the RMS vorticity of the 2D comparison flow in figure 2(d). (The 3D flow has more RMS vorticity than the 2D flow, but less than the maximum permitted by (7.2).) Moreover, all numerical and experimental results indicate that $\bar{b}(0) \rightarrow -b_\star$ as $Ra \rightarrow \infty$. Thus increasing Ra above 6.4×10^{13} likely reduces the already small 8% difference between the RMS vorticity of the 3D flow and the 2D comparison flow. The small enhancement of 3D RMS vorticity implies that vortex stretching (c) does not effectively operate in 3D HC.

As a concluding illustration of the vorticity bound (7.2), notice that in figures 1 and 2 the vorticity is scaled with $\sqrt{b_\star/h}$. With this scaling the same colorbar applies even as Ra is varied by a factor 10^6 . The vorticity of the 3D flow in figure 9 is also scaled with $\sqrt{h/b_\star}$. This simple estimate of the RMS vorticity applies across all 2D and 3D solutions reported here.

8. Conclusion

We have conducted a numerical study of the Ra - Nu relation with $Pr = 1$ and four cases corresponding to either no-slip or free-slip boundary conditions, in both 2D ($\ell_y/h = 0$) or 3D ($\ell_y/h = 1$) geometries. In all four cases, with Ra in the range 10^6 to 10^{10} , we find that heat flux obeys Rossby scaling, that is, $Nu \sim Ra^{1/5}$. In the 2D cases, with maximum Rayleigh

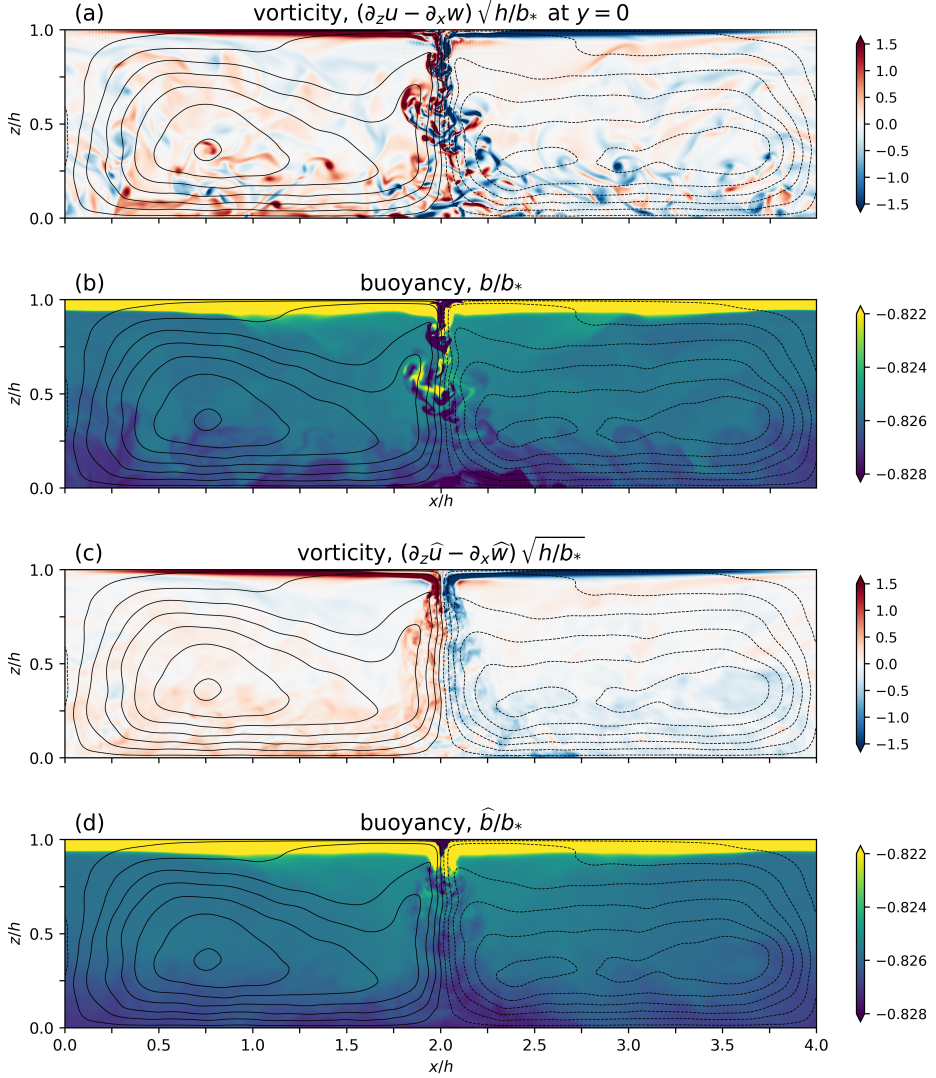


Figure 9: Panels (a) and (b) show a y -slice of snapshots of 3DFS HC at $Ra = 3.20 \times 10^{11}$. The spanwise averages of the snapshots of vorticity and buoyancy are shown in panels (c) and (d). In all panels, the contours are streamlines computed from a spanwise averaged snapshot at the final time. At the top surface $-1 \leq b/b_* \leq +1$; the narrow range of the buoyancy color scale makes the small interior variations visible.

number of order 10^{14} , we found that a scaling regime with $Nu \sim Ra^{1/4}$ replaces the Rossby scaling for Ra beyond 10^{11} ; see also Tsai *et al.* (2020).

The scaling arguments for the $Nu-Ra$ relation of HC reviewed in section 4 do not depend very much, if at all, on the distinction between 2D and 3D HC. Nor do these arguments identify the spanwise aspect ratio ℓ_y/h as an important parameter. Thus it is informative to conduct parallel numerical studies of 2D and 3D HC and compare corresponding Nu 's. This comparison of 2D with 3D HC, extending to $Ra = 3.2 \times 10^{11}$, shows that 3D HC has only a slight 10 or 20% enhancement of heat transport over non-turbulent 2D HC. It is difficult to believe that there is only a slight enhancement at significantly higher Ra – otherwise relatively inexpensive 2D numerical solutions would provide useful estimates of 3D HC heat transport.

It is likely that the 2D Nu is less than (or equal to) the 3D Nu . Proving this plausible conjecture is an open challenge.

Our results, numerical and theoretical, reinforce the view that HC does not express all of the characteristics of turbulence (Paparella & Young 2002).

Acknowledgments

Without implying their endorsement, we thank Basile Gallet and Ross Griffiths for discussions of horizontal convection. Computational resources were provided by the Australian National Computational Infrastructure at the Australian National University, which is supported by the Commonwealth of Australia. NCC was supported by the Australian Research Council DECRA Fellowship DE210100749. CBR was supported by National Aeronautics and Space Administration Award NNX16AO5OH. SGLS was partially supported by National Science Foundation Awards OCE-1829919 WRY was supported by National Science Foundation Awards OCE-1657041 and OCE-2048583.

Appendix A. The low Rayleigh number regime

If the Rayleigh number is sufficiently small then one can employ a straightforward expansion in powers of Ra to show that the Nusselt number is

$$Nu = 1 + C_2 Ra^2 + \text{ord}(Ra^4). \quad (\text{A } 1)$$

In the expansion (A 1), C_2 is a function of the aspect ratio, $A_x = \ell_x/h$, but not the Prandtl number Pr . In this appendix we summarize the calculation of C_2 for horizontal convection forced with the sinusoidal b_s in (2.4). This calculation is more interesting than one might anticipate because C_2 turns out to be a very small number for all values of the aspect ratio A_x . Consequently with the aspect ratio $A_x = 4$ used in this work “sufficiently small” means Rayleigh numbers of order 10^4 (see the inset in figure 4).

Using the streamfunction formulation, with $(u, w) = (-\psi_z, \psi_x)$, and scaling lengths with the depth h and time with h^2/κ the steady Boussinesq equations are

$$\psi_x \nabla^2 \psi_z - \psi_z \nabla^2 \psi_x = b_x + Pr \nabla^4 \psi, \quad (\text{A } 2)$$

$$\psi_x b_z - \psi_z b_x = \nabla^2 b, \quad (\text{A } 3)$$

where here $\nabla^2 = \partial_x^2 + \partial_z^2$ is the two-dimensional Laplacian; the spanwise vorticity is $u_z - w_x = -\nabla^2 \psi$. The surface boundary condition is $b(x, 1) = \epsilon \cos mx$ where

$$m \stackrel{\text{def}}{=} kh = 2\pi/A_x, \quad \text{and} \quad \epsilon \stackrel{\text{def}}{=} PrRa/A_x^3 = PrRa (m/2\pi)^3. \quad (\text{A } 4)$$

We expand all variables in powers of the small parameter ϵ

$$(b, \psi) = \epsilon(b_1, \psi_1) + \epsilon^2(b_2, \psi_2) + \dots \quad (\text{A } 5)$$

The first-order equations are

$$Pr \nabla^4 \psi_1 = -b_{1x}, \quad \text{and} \quad \nabla^2 b_1 = 0. \quad (\text{A } 6)$$

The solution (A 6) is

$$\psi_1 = \sin mx P(z), \quad \text{and} \quad b_1 = \cos mx B(z), \quad (\text{A } 7)$$

where $B(z) \stackrel{\text{def}}{=} \text{sech } m \cosh mz$. In $\psi_1(x, z)$ we have the free-slip function

$$P^{FS}(z) = \frac{B(z)}{8m^2 Pr} [(m \coth m + 1 - z) \tanh mz - mz(2 - z)], \quad (\text{A } 8)$$

and the no-slip function

$$P^{\text{NS}}(z) = \frac{1}{8mPr(\sinh^2 m - m^2)} \left[(\sinh^2 m - m^2)(z^2 - z)B(z) + (\tanh m - m)z \sinh m(1 - z) + (\sinh m - m \operatorname{sech} m)(1 - z) \sinh mz \right]. \quad (\text{A } 9)$$

At second order in ϵ we must solve

$$\nabla^2 b_2 = \psi_{1x} b_{1z} - \psi_{1z} b_{1x}, \quad (\text{A } 10)$$

$$= \underbrace{\frac{1}{2}m(PB)'}_{J_0} + \underbrace{\frac{1}{2}m(PB' - P'B)}_{J_2} \cos 2mx. \quad (\text{A } 11)$$

The solution of (A 11) has the form

$$b_2 = B_{20}(z) + B_{22}(z) \cos 2mx, \quad (\text{A } 12)$$

where B_{20} and B_{22} are determined by solving

$$B''_{20} = J_0, \quad (\text{A } 13)$$

$$B''_{22} - 4m^2 B_{22} = J_2. \quad (\text{A } 14)$$

Forming $\langle B_{22} \rangle$ (A 14) we find the shortcut used below in passing from (A 16) to (A 17):

$$\left\langle B'_{22}^2 + 4m^2 B_{22}^2 \right\rangle = -\langle B_{22} J_2 \rangle. \quad (\text{A } 15)$$

The expressions for B_{22} and B_{20} , obtained with Mathematica, are complicated and are not explicitly presented. Mercifully, to obtain the coefficient C_2 in (A 1), we do not need ψ_2 .

Multiplying $\nabla^2 b_1 = 0$ by b_n , with $n \geq 2$, and noting that all these b_n 's have homogeneous boundary conditions at $z = 0$ and 1 , we see that $\langle \nabla b_n \cdot \nabla b_1 \rangle = 0$. Consequently the expansion of the buoyancy variance dissipation is

$$\chi = \underbrace{\epsilon^2 \langle |\nabla b_1|^2 \rangle}_{\chi_2 = \frac{1}{2}m \tanh m} + \underbrace{\epsilon^4 \langle |\nabla b_2|^2 \rangle}_{\chi_4} + \operatorname{ord}(\epsilon^6). \quad (\text{A } 16)$$

Recalling the definition of ϵ in (A 4), the Nusselt number is

$$Nu = 1 + \underbrace{\frac{m^2 \langle (PB)^2 \rangle - 2\langle B_{22} J_2 \rangle}{2m \tanh m}}_{\chi_4/\chi_2} \left(\frac{m^3 Pr}{8\pi^3} \right)^2 Ra^2 + \dots. \quad (\text{A } 17)$$

Because P , B_{22} , and J_2 are all proportional to Pr^{-1} , the Prandtl number Pr cancels out of the coefficient of Ra^2 in (A 17).

With FS boundary conditions, the expression for C_2 in (A 1) is

$$C_2^{\text{FS}} = \left[690 - 1920m^4 \operatorname{cosech}^2 m + 20(3 + 4m^2)^2 \operatorname{sech} 2m + m(1024m^4 - 80m^2 - 6195) \operatorname{cosech} m \operatorname{sech}^3 m + 5(352m^4 - 624m^2 + 1065) \operatorname{sech}^2 m \right] / 41\,943\,040\,\pi^6. \quad (\text{A } 18)$$

Limiting values in the FS case are

$$\lim_{m \rightarrow 0} C_2^{\text{FS}} = \frac{31 m^8}{30965760\pi^6} + \text{ord}(m^{10}), \quad (\text{A } 19)$$

and

$$\lim_{m \rightarrow \infty} C_2^{\text{FS}} = \frac{69}{4194304\pi^6}. \quad (\text{A } 20)$$

We admire the frequently occurring integer $4194304 = 2^{22}$ in the formulas above and below.

With NS boundary conditions, we find

$$C_2^{\text{NS}} = \frac{1}{41943040\pi^6} \frac{\Xi(m)}{(\cosh 2m - 2m^2 - 1)^2}, \quad (\text{A } 21)$$

where

$$\begin{aligned} \Xi(m) = & 85 \cosh 4m - 320m(33 + 8m^2) \sinh 2m + 10(845 + 716m^2) \cosh 2m \\ & - 5(5123 + 18304m^2 + 13720m^4 + 2912m^6) \\ & - 4m^5(7215 + 100m^2 - 64m^4) \coth m \\ & + 20(829 + 4402m^2 + 5289m^4 + 836m^6 - 64m^8) \operatorname{sech}^2 m \\ & - 4m(4785 + 8010m^2 + 1549m^4 - 212m^6 + 64m^8) \tanh m \operatorname{sech}^2 m \\ & + 20(25 - 184m^2 - 80m^4 - 16m^6) \operatorname{sech} 2m \\ & + 4m(8865 + 21640m^2 + 17719m^4 + 740m^6 - 64m^8) \tanh m \\ & + 160m(15 - 7m^2 - 4m^4) \tanh 2m. \end{aligned} \quad (\text{A } 22)$$

Limiting values in the NS case are

$$\lim_{m \rightarrow 0} C_2^{\text{NS}} = \frac{m^8}{30965760\pi^6} + \text{ord}(m^{10}), \quad (\text{A } 23)$$

and

$$\lim_{m \rightarrow \infty} C_2^{\text{NS}} = \frac{17}{4194304\pi^6}. \quad (\text{A } 24)$$

It is notable that the small- m C_2^{NS} in (A 23) is smaller by a factor of exactly 31 than C_2^{FS} in (A 19).

Both C_2 's are very much less than one for all aspect ratios. In the numerical solutions summarized in figure 4, the aspect ratio is $A_x = 4$, corresponding to $m = kh = \pi/2$. The results in (3.3) and (3.4) follow by evaluating the formulas (A 18) through (A 22) with $m = \pi/2$.

REFERENCES

- BENZI, R., PATARNELLO, S & SANTANGELO, P 1987 On the statistical properties of two-dimensional decaying turbulence. *Europhys. Lett.* **3** (7), 811.
- BENZI, R., PATARNELLO, S & SANTANGELO, P 1988 Self-similar coherent structures in two-dimensional decaying turbulence. *J. Phys. A* **21** (5), 1221.
- BURNS, K. J., VASIL, G. M., OISHI, J. S., LECOANET, D. & BROWN, B. P. 2020 Dedalus: A flexible framework for numerical simulations with spectral methods. *Phys. Rev. Res.* **2**, 023068.
- CARNEVALE, G. F., McWILLIAMS, J. C., POMEAU, Y., WEISS, J. B. & YOUNG, W. R. 1991 Evolution of vortex statistics in two-dimensional turbulence. *Phys. Rev. Lett.* **66** (21), 2735.
- CHIU-WEBSTER, S., HINCH, E. J. & LISTER, J. R. 2008 Very viscous horizontal convection. *J. Fluid Mech.* **611**, 395–426.

- COMAN, M. A., GRIFFITHS, R. W. & HUGHES, G. O. 2006 Sandström's experiments revisited. *J. Mar. Res.* **64** (6), 783–796(14).
- DRITSCHEL, D. G., SCOTT, R. K., MACASKILL, C., GOTZWALD, G. A. & TRAN, C. V. 2008 Unifying scaling theory for vortex dynamics in two-dimensional turbulence. *Phys. Rev. Lett.* **101** (9), 094501.
- GAYEN, B., GRIFFITHS, R. W. & HUGHES, G. O. 2014 Stability transitions and turbulence in horizontal convection. *J. Fluid Mech.* **751**, 698–724.
- GAYEN, B., GRIFFITHS, R. W., HUGHES, G. O. & SAENZ, J. A. 2013 Energetics of horizontal convection. *J. Fluid Mech.* **716**, R10.
- HUGHES, G. O. & GRIFFITHS, R. W. 2008 Horizontal convection. *Annu. Rev. Fluid Mech.* **40**, 185–208.
- ILICAK, M. & VALLIS, G. K. 2012 Simulations and scaling of horizontal convection. *Tellus A* **64** (1), 18377.
- KUHLBRODT, T. 2008 On Sandström's inferences from his tank experiments: a hundred years later. *Tellus A* **60** (5), 819–836.
- MCWILLIAMS, J. C 1984 The emergence of isolated, coherent vortices in turbulent flow. *J. Fluid Mech.* **146**, 21–43.
- MCWILLIAMS, J. C 1990 The vortices of two-dimensional turbulence. *J. Fluid Mech.* **219**, 361–385.
- MULLARNEY, J. C., GRIFFITHS, R. W. & HUGHES, G. O. 2004 Convection driven by differential heating at a horizontal boundary. *J. Fluid Mech.* **516**, 181–209.
- NCFMF 1968 Turbulence (Educational film from 1968). <https://youtu.be/AeBsiEYWZUY>.
- NCFMF 1972 *Illustrated Experiments in Fluid Mechanics: The NCFMF Book of Film Notes. National Committee for Fluid Mechanics Films*. MIT Press.
- PAPARELLA, F. & YOUNG, W. R. 2002 Horizontal convection is non-turbulent. *J. Fluid Mech.* **466**, 205–214.
- PASSAGGIA, PIERRE-YVES, SCOTTI, ALBERTO & WHITE, BRIAN 2017 Transition and turbulence in horizontal convection: linear stability analysis. *J. Fluid Mech.* **821**, 31–58.
- ROCHA, C. B., BOSSY, T., LLEWELLYN SMITH, S. G. & YOUNG, W. R. 2020a Improved bounds on horizontal convection. *J. Fluid Mech.* **883**, A41.
- ROCHA, C. B., CONSTANTINOU, N. C., LLEWELLYN SMITH, S. G. & YOUNG, W. R. 2020b The Nusselt numbers of horizontal convection. *J. Fluid Mech.* **894**, A24.
- ROSSBY, H. T. 1965 On thermal convection driven by non-uniform heating from below: an experimental study. *Deep Sea Res.* **12** (1), 9–10, IN9–IN14, 11–16.
- ROSSBY, H. T. 1998 Numerical experiments with a fluid heated non-uniformly from below. *Tellus A* **50** (2), 242–257.
- SANDSTRÖM, J. W. 1908 Dynamische versuche mit meerwasser. *Annals in Hydrodynamic Marine Meteorology* **36**, 6–23.
- SCOTTI, A. & WHITE, B. 2011 Is horizontal convection really “non-turbulent?”. *Geophys. Res. Lett.* **38** (21), L21609.
- SHEARD, G. J. & KING, M. P. 2011 Horizontal convection: effect of aspect ratio on Rayleigh number scaling and stability. *Appl. Math. Modelling* **35** (4), 1647–1655.
- SHISHKINA, O., GROSSMANN, S. & LOHSE, D. 2016 Heat and momentum transport scalings in horizontal convection. *Geophys. Res. Lett.* **43** (3), 1219–1225.
- SIGGERS, J. H., KERSWELL, R. R. & BALMFORTH, N. J. 2004 Bounds on horizontal convection. *J. Fluid Mech.* **517**, 55–70.
- TAYLOR, G. I. 1938 Production and dissipation of vorticity in a turbulent fluid. *Proc. R. Soc. Lond. A* **164** (916), 15–23.
- TAYLOR, G. I. & GREEN, A. E. 1937 Mechanism of the production of small eddies from large ones. *Proc. R. Soc. Lond. A* **158** (895), 499–521.
- TSAI, T., HUSSAM, W. K., FOURAS, A. & SHEARD, G. J. 2016 The origin of instability in enclosed horizontally driven convection. *Int. J. Heat and Mass Transfer* **94**, 509–515.
- TSAI, T., HUSSAM, W. K., KING, M. P. & SHEARD, G. J. 2020 Transitions and scaling in horizontal convection driven by different temperature profiles. *Int. J. Thermal Sci.* **148**, 106166.
- WANG, W. & HUANG, R. X. 2005 An experimental study on thermal convection driven by horizontal differential heating. *J. Fluid Mech.* **540**, 49–73.
- WINTERS, K. B. & YOUNG, W. R. 2009 Available potential energy and buoyancy variance in horizontal convection. *J. Fluid Mech.* **629**, 221–230.